Journal of Computers Vol. 33 No. 4, August 2022, pp. 225-236
doi: 10.53106/199115992022083304019

Research on Drag Reduction Mechanism of Supersonic Ship Tail-shaped Projectile Based on Computer-aided Simulation

Chao Song, Zi-Qiang Xiao*, Yi-Zhuo Jia, Hai Lin, Bing Ji

Department of Weapons and Control, Army Academy of Armored Forces, Beijing, China
andysong475@163.com

Received 1 June 2022; Revised 8 July 2022; Accepted 8 August 2022

Abstract: In order to quantitatively study the influence of the shape of the stern on the resistance of the projectile, the computer-aided fluid dynamics method was used to numerically analyze the shape of the stern model with different mach numbers under the condition of supersonic speed, by analyzing and comparing the pressure coefficient distribution of the stern flow field, the stern surface and the bottom of the projectile ship. The results showed that the tail resistance of the projectile increases linearly with the increase of the tail cone angle; the bottom resistance of the projectile is affected by the area of the bottom of the projectile (shrinkage ratio) and the tail cone angle, and increases linearly with the increase of the shrinkage ratio; The overall drag coefficient of the projectile is related to the bottom resistance and the tail resistance. When the tail length is fixed, there is a tail cone angle that minimizes the drag coefficient, and its size is related to the flight speed of the projectile. When the flight speed of the arrow increases to 3Ma, the optimal solution of the tail cone angle reaches a stable value and its value is about 9.8°, which has a certain reference value for the design of the aerodynamic shape of the high Mach number arrow.

Keywords: computer-aided fluid dynamics method, projectile boattail, drag coefficient, aerodynamic characteristics, pressure coefficient, supersonic

1 Introduction

The aerodynamic performance of artillery-launched ammunition is one of the most important performances of artillery. Researchers can increase the range of the artillery by reducing the resistance of the projectile body, which is an important means to increase the combat efficiency of artillery [1]. The main air resistance of the projectile body includes three parts [2]: 1. The wave resistance mainly produced by the projectile body wave; 2. Friction caused by air viscous friction; 3. The bottom resistance caused by the bottom low pressure formed by the separation of the bottom fluid of the projectile. The formation of the bottom resistance of the projectile is mainly due to the separation of the boundary layer. The boundary layer is a thin flow layer with a non-negligible viscous force close to the surface of the flow around the high Reynolds number [3]. After the separation of the boundary layer, alternate shedding vortices will be formed. A low pressure zone will be formed in the vortex zone, which will increase the resistance of the pressure difference between the front and rear of the projectile, so the bottom resistance is also called vortex resistance. At the same time, the separation of the boundary layer will also cause the loss of mechanical energy of the fluid, and the speed loss of the bullet for the bullet. In severe cases, the stability of the bullet will decrease and the shooting accuracy will be affected. Generally, there are two reasons for the separation of the projectile boundary layer and the projectile to form vortex resistance: one is that the flow rate is constant, and the rear section of the projectile changes sharply; the other is that the shape of the projectile changes little after the largest section, but the airflow velocity is larger [4].

With the gradual optimization of the aerodynamic shape of projectiles and rockets, a large number of methods for bottom drag reduction have been proposed by researchers. There are two main ideas: one is to make the bottom pressure of the projectile drop as little as possible when the low pressure zone is formed, such as a ship-shaped projectile. Tail [5] and bottom concave bullets [6]; the other is to add gas to the low pressure area (vortex area) at the bottom of the bullet, thereby increasing the bottom pressure of the bullet and realizing the drag reduction and range extension of the artillery, such as the bottom row of bullets [7-8].

In recent years, with the development of computational fluid dynamics (CFD), the analysis of the bottom pressure and flow field characteristics of projectiles and rockets has become more in-depth, providing a basis for

* Corresponding Author

the refinement of the aerodynamic characteristics of the stern of projectiles and rockets. Based on the SCOBT projectile model, this paper uses slip grid and technology to establish a three-dimensional flow field model of the projectile body. The projectiles flying at supersonic speed under rotating conditions are studied, and the influence of different ship stern structures on the aerodynamic performance of the projectile body is analyzed. The characteristics of the flow field around the stern stern reveals the drag reduction mechanism of the stern stern under supersonic conditions. The changes in the tail resistance, bottom resistance and the overall drag coefficient of the projectile are studied when the shape of the stern changes.

2 Numerical Simulation Method

2.1 Governing Equation and Its Discrete Format

For the rotationally stable artillery projectile, its flow field around the flow has a high degree of axial symmetry, so the Reynolds time-averaged Navier-Stokes equation in the form of differential conservation is used as the governing equation [9]:

$$\frac{\partial \boldsymbol{U}}{\partial t}+\frac{\partial \boldsymbol{F}}{\partial x}+\frac{\partial \boldsymbol{G}}{\partial y}+\frac{\partial \boldsymbol{H}}{\partial z}=\frac{\partial \boldsymbol{F}_V}{\partial x}+\frac{\partial \boldsymbol{G}_V}{\partial y}+\frac{\partial \boldsymbol{H}_V}{\partial z} \tag{1}$$

Where: $\boldsymbol{U}$ is a conserved variable; $\boldsymbol{F}$, $\boldsymbol{G}$, and $\boldsymbol{H}$ are inviscid convective vector fluxes; $\boldsymbol{F}_V$, $\boldsymbol{G}_V$, and $\boldsymbol{H}_V$ are viscous convective fluxes; each expression is as follows:

$$\boldsymbol{U}=\begin{bmatrix}\rho\\ \rho u\\ \rho v\\ \rho w\\ \rho e\end{bmatrix},\boldsymbol{F}=\begin{bmatrix}\rho u\\ \rho u^2+P\\ \rho uv\\ \rho uw\\ (\rho e+p)u\end{bmatrix},\boldsymbol{G}=\begin{bmatrix}\rho v\\ \rho uv\\ \rho v^2+p\\ \rho vw\\ (\rho e+p)v\end{bmatrix}$$

$$\boldsymbol{H}=\begin{bmatrix}\rho w\\ \rho uw\\ \rho vw\\ \rho w^2+p\\ (\rho e+p)w\end{bmatrix},\boldsymbol{F}_V=\begin{bmatrix}0\\ \tau_{xx}\\ \tau_{yx}\\ \tau_{zx}\\ \tau_{xx}u+\tau_{xy}v+\tau_{xz}w-q_x\end{bmatrix}$$

$$\boldsymbol{G}_V=\begin{bmatrix}0\\ \tau_{xy}\\ \tau_{yy}\\ \tau_{zy}\\ \tau_{yx}u+\tau_{yy}v+\tau_{yz}w-q_y\end{bmatrix}$$

$$\boldsymbol{H}_V=\begin{bmatrix}0\\ \tau_{xz}\\ \tau_{yz}\\ \tau_{zz}\\ \tau_{xz}u+\tau_{yz}v+\tau_{zz}w-q_z\end{bmatrix}$$

Where: ρ is the fluid density; p is the pressure term; e is the total energy per unit volume; u, v, and w are the speeds in the x, y and z directions; x is the flow direction; $\tau_{\xi\eta}(\xi,\eta=x,y,z)$ is viscous stress; q_x, q_y, and q_z are the heat flow of heat conduction.

The spatial discretization format adopts the second-order upwind style, and the solver uses a coupled explicit algorithm based on density basis. The fluid separation phenomenon at the bottom of the bullet and the bottom vortex make the turbulence at the bottom of the bullet show a high degree of nonlinearity. Therefore, the turbulence model adopts the RNG $k-\varepsilon$ model [10]. The $k-\varepsilon$ model is a typical two-equation model. It is based on the one-equation model. After introducing an equation about the turbulence dissipation rate, it is the most widely used turbulence model at present. The RNG model is improved on the basis of the standard model. The RNG $k-\varepsilon$ model can handle high strain rates and streamlines well. Flow with a greater degree of curvature. The RNG $k-\varepsilon$ model mainly includes turbulent kinetic energy k equation and turbulent dissipation rate ε equation, where turbulent viscosity μ_t is expressed as a function k of the turbulent kinetic energy:

$$\mu_t = \rho C_\mu \sqrt{kl} \tag{2}$$

Where: σ_k and C_μ is empirical constant, l is the length along the streamline.

The turbulent kinetic energy k equation is:

$$\varepsilon = \frac{\mu}{\rho}\overline{\left(\frac{\partial u_i'}{\partial x_k}\right)\left(\frac{\partial u_j'}{\partial x_k}\right)} \tag{3}$$

According to the above equation (2) and equation (3), the transport equation of the standard model is:

$$\frac{\partial(\rho \mathrm{k})}{\partial t}+\frac{\partial\left(\rho k u_i\right)}{\partial x_i}=\frac{\partial}{\partial x_i}\left[\left(\mu+\frac{\partial \mu_t}{\sigma_k}\right)\right]+G_k+G_d-\rho\varepsilon-Y_M+S_k \tag{4}$$

$$\frac{\partial(\rho \varepsilon)}{\partial t}+\frac{\partial\left(\rho \varepsilon u_i\right)}{\partial x_i}=\frac{\partial}{\partial x_j}\left[\left(\mu+\frac{\partial \mu_t}{\sigma_\varepsilon}\right)\frac{\partial \varepsilon}{\partial x_j}\right]+C_{1\varepsilon}\frac{\varepsilon}{k}\left(G_k+C_{2\varepsilon}G_b\right)-C_{2\varepsilon}\rho\frac{\varepsilon^2}{k}+S_\varepsilon \tag{5}$$

Where: G_k is the generation term of turbulent kinetic energy caused by mean velocity gradient; μ is the turbulent viscosity; Y_M is the pulse expansion term in compressible turbulence; $C_{1\varepsilon}$, $C_{2\varepsilon}$ and $C_{3\varepsilon}$ are empirical constants; S_ε and S_k are user-defined source items.

2.2 Computational Model and Boundary Conditions

The calculation model uses a 6-fold caliber projectile named SOCBT [11]. This model has the most typical gun-launched ammunition structure, that is, the projectile is composed of three parts: the arc part, the cylindrical part and the stern part. Due to its typical shape structure, SOCBT is widely used as the basic projectile for the study of aerodynamic shape [12]. Based on the standard SOCBT, the relevant parameters of stern, bottom concave and bottom jet are adjusted. The calculation model is shown in Fig. 1.

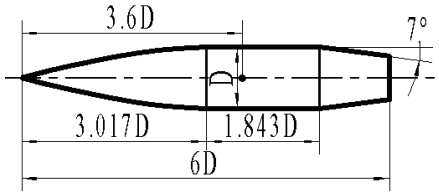

Fig. 1. The model of SOCBT projectile

The calculation is completed by the computational fluid dynamics (CFD) software fluent, and the grid adopts an unstructured grid. In order to ensure the accuracy of the calculation, the grid at the tip and the tail of the bullet is refined, and The grid height of the first layer of the boundary layer is given according to $y^{+}\leq 1$. The projectile's mesh is shown in Fig. 2.

Fig. 2. Projectile surface mesh

In order to simulate the rotation effect of the projectile, the sliding mesh technology is used, the principle of which is shown in Fig. 3. The principle of the sliding mesh to simulate the rotating motion of the projectile is to divide the flow field into two parts: the dynamic domain and the static domain. Data is exchanged between the dynamic domain and the static domain through the interface, and the rotational speed of the dynamic domain is the rotational speed of the projectile during flight. The dimensionless rotational speed of the projectile $\omega=0.19(\omega=\omega_0 d/v_\infty)$. The overall computational mesh model and boundary conditions are shown in Fig. 4.

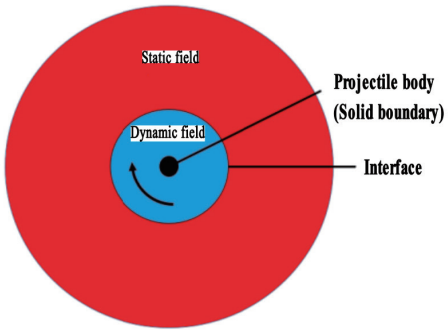

Fig. 3. Schematic diagram of slip grid principle

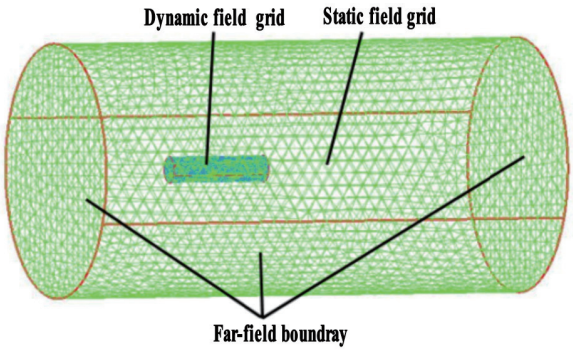

Fig. 4. Overall computing grid

2.3 Algorithm Verification

In order to verify the validity and reliability of the numerical calculation method established in this paper in the aerodynamic simulation of high-speed rotating projectiles, the simulation method is first verified by referring to the SOCBT experimental data in [13]. The curve shown in Fig. 5 represents the surface pressure coefficient of the projectile at an incoming Mach number of 0.94 and an angle of attack of 0°:

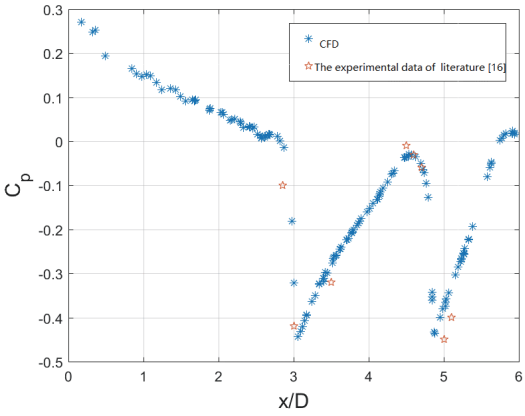

Fig. 5. Projectile pressure coefficient curve

It can be seen from the curve in Fig. 5 that the numerical calculation is consistent with the pressure coefficient variation law obtained by the wind tunnel experiment. Although there is a certain error, the relative error is within the allowable range, indicating that the numerical simulation method established in this paper is accurate. In this paper, according to the above model, the parameters affecting the resistance coefficient of ammunition are numerically analyzed and some laws are obtained.

3. Stern-shaped Projectile Tail

The drag coefficient of the stern-shaped projectile tail consists of two parts, one is the drag coefficient of the conical part of the tail (called tail drag), and the other part is the drag coefficient of the bottom part of the projectile (called projectile drag). Fig. 6 is a schematic diagram of the flow field at the tail of the projectile. The flow state at the bottom of the projectile can be divided into three areas, the free flow area, the bottom recirculation area and the shear layer area.

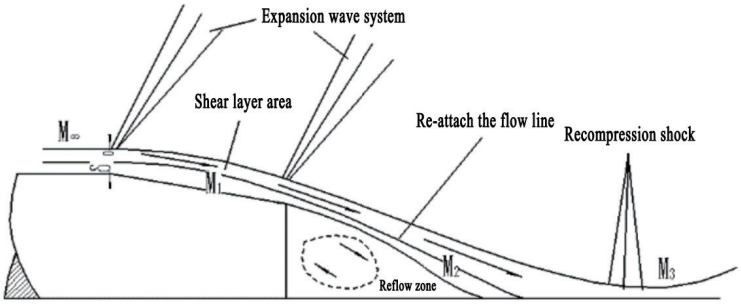

Fig. 6. Schematic diagram of the flow field at the tail of the projectile

Under the condition of supersonic incoming flow, due to the influence of air viscosity, there is a thin boundary layer (boundary layer) on the surface of the projectile. The bottom recirculation area surrounded by the shear layer developed by the separation of the boundary layer, the velocity of the airflow in this area is very small, and the pressure in this area is very low due to the mixing and ejection of airflow [14]. The shear layer area is the transi-

tion area connecting the free flow area and the bottom recirculation area. The flow state of the shear layer area has a great influence on the bottom recirculation area. The separation streamline is the airflow boundary line between the outflow area and the shear layer area. The shape of the separation streamline directly affects the velocity and pressure distribution in the outflow area, and the velocity and pressure distribution in the outflow area affect the pressure in the bottom recirculation area through the shear layer area. and bottom resistance. Therefore, the gas flow state and bottom pressure at the bottom of the arrow have a great relationship with the state of the shear layer. Theoretical analysis and experiments show that the shear layer state must be changed to increase the bottom pressure. The straighter the separation streamline, the greater the expansion angle. Smaller, the higher the bottom pressure, the smaller the bottom resistance [15]. The change of the stern cone angle directly affects the flow state of the shear layer, thereby affecting the resistance characteristics of the projectile tail. It directly affects the effect of the bottom pressure on the arrow.

4 Numerical Simulation

4.1 Analysis of the Flow Field at the Tail of the Projectile

Fig. 7 shows the velocity cloud diagram of the flow field around the projectile with different tail cone angles when the incoming flow is 2.5 Ma. It can be seen that the tail of the projectile forms an obvious expansion wave at the connection of the cylindrical part. With the increase of the tail cone angle, the cylindrical and the speed difference between the tail and the tail of the projectile gradually increases [16]. According to the Prandtl-Meyer theory, as the angle of the airflow increases, the velocity difference before and after the angle increases gradually, and there is a limit angle. When the angle of the geometry is larger than this angle, the airflow will not remain attached to the surface of the object. The bottom forms a bottom recirculation area surrounded by the shear layer developed by the separation of the boundary layer, and the velocity of the airflow in this area is very small.

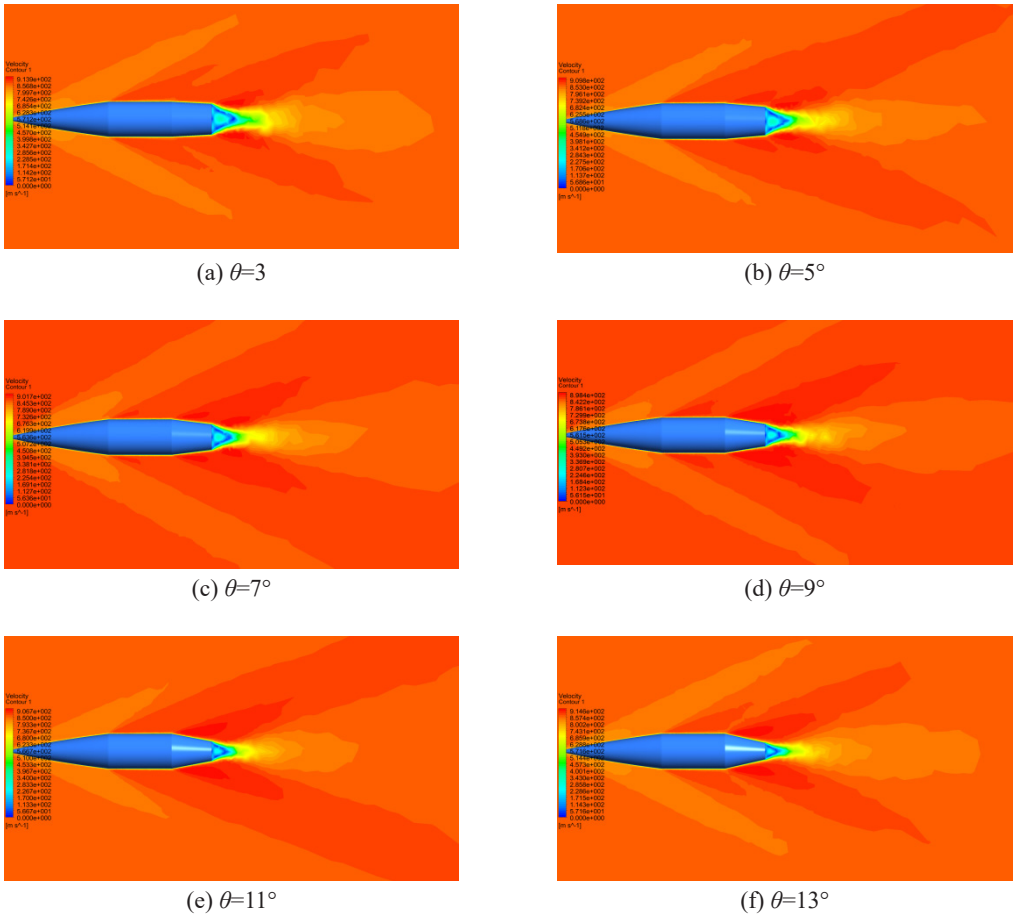

(a) θ=3 (b) θ=5°

(c) θ=7° (d) θ=9°

(e) θ=11° (f) θ=13°

Fig. 7. Velocity cloud map under different tail cone angles

It can be seen from Fig. 7 that with the increase of the tail cone angle θ of the projectile, the range of the turbulent region formed by the tail of the projectile gradually decreases, and it can be clearly seen that the range of the turbulent region at the tail of the projectile increases with the increase of the tail cone angle. The obvious decrease is mainly due to the fact that the tail cone angle causes an expansion wave to form at the tail of the projectile [17], the airflow velocity at the tail of the projectile increases, and the airflow angle is larger, resulting in the earlier intersection of the airflow after the angle of the tail of the projectile, thus reducing the turbulent area at the tail of the projectile. small, which also reduces the negative pressure area at the bottom of the projectile.

4.2 Projectile Pressure Distribution

In order to further reveal the influence of the change of the tail cone angle on the pressure of the projectile tail, the pressure coefficient C_p of the projectile tail is analyzed below.

4.2.1 Projectile Bottom Pressure

Fig. 8 shows the distribution curve of the pressure coefficient C_p at the bottom of the projectile when the shrinkage ratio is constant and the tail cone angle θ is different. It can be seen that the absolute value of the pressure coefficient at the axis of the projectile is the smallest. This is because in the return zone at the bottom of the projectile, the air flows towards the bottom of the projectile, stagnates at the axis of the projectile bottom and flows along the radial direction, resulting in the center of the projectile bottom. where the pressure is the largest, the velocity vector diagram of the tail of the projectile is shown in Fig. 9.

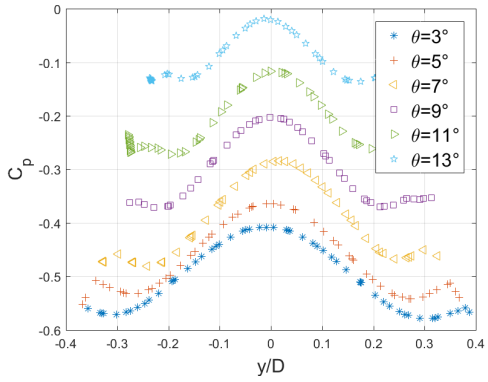

(a) Ma=1.5

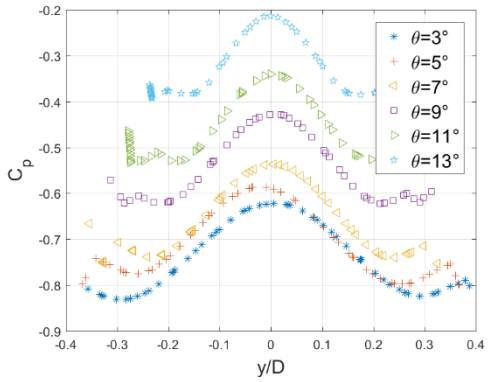

(b) Ma=2

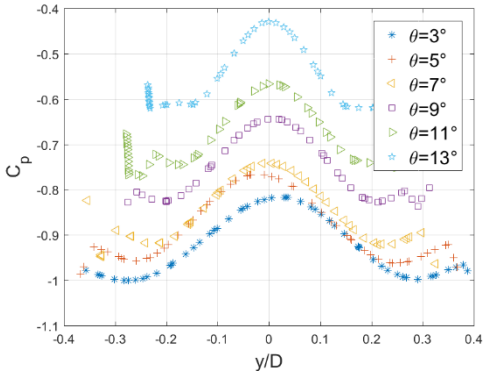

(c) Ma=2.5

Fig. 8. Bottom pressure coefficient C_p distribution curve

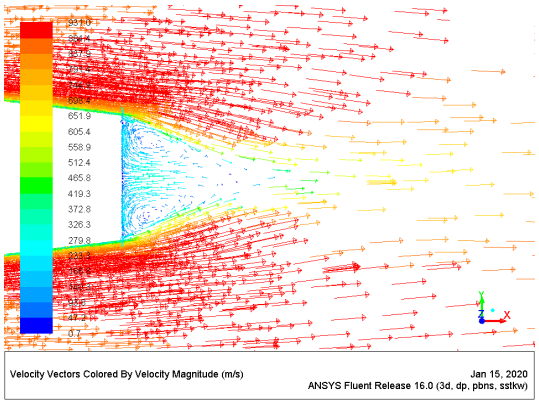

Fig. 9. Projectile tail velocity vector diagram (2Ma, θ=7°, arrows indicate velocity)

It can be seen from Fig. 8 that with the increase of the tail cone angle θ, the pressure coefficient C_p of the projectile bottom shows an overall increasing trend, that is, the absolute value of C_p gradually decreases, which means that the negative pressure of the projectile bottom gradually decreases. Small, the bottom pressure of the projectile gradually increases, and at the same time, due to the gradual increase of the tail cone angle, the bottom area of the projectile decreases when the diameter of the projectile does not change. Under the combined action of pressure reduction and projectile bottom area reduction, the projectile bottom resistance decreases gradually with the increase of tail cone angle. At the same time, with the increase of Ma, the absolute value of the pressure coefficient at the bottom of the projectile gradually increases, which means that with the increase of the number of Ma, the bottom resistance of the projectile gradually increases.

4.2.2 Projectile Pressure

Fig. 10 is the distribution curve of the projectile pressure coefficient C_p under different tail cone angles and Ma. It can be seen that since the cylindrical part of the projectile and the head of the projectile do not change significantly, the pressure coefficients are basically the same.

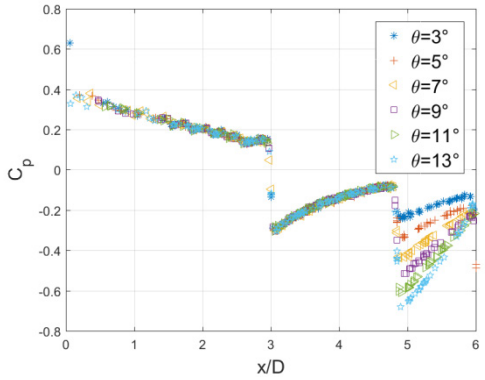

(a) Ma=1.5

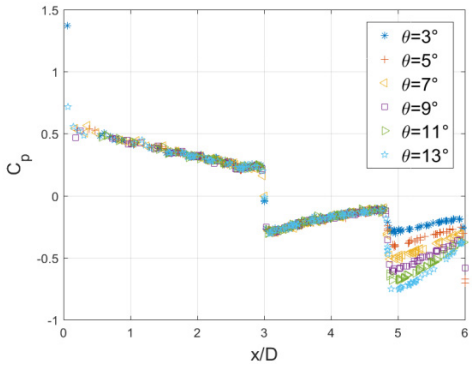

(b) Ma=2

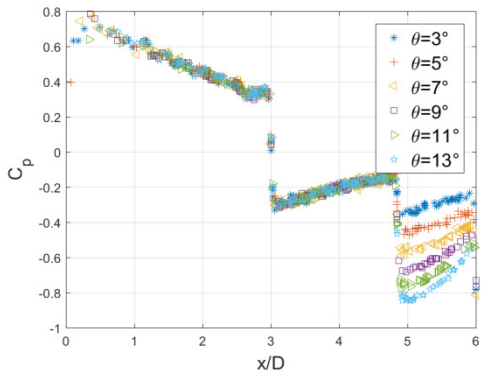

(c) Ma=2.5

Fig. 10. Projectile pressure coefficient C_p distribution curve

As shown in Fig. 10, there are two sudden changes in the C_p distribution curve of the projectile pressure coefficient under different Ma numbers. This is due to the sudden change of shape at the connection between the projectile head and the projectile tail and the cylindrical part, which makes the surface of the projectile expand. There are large changes in the airflow velocity and pressure before and after the wave.

For different tail cone angles θ, with the increase of the tail cone angle, the sudden change of the pressure coefficient curve at the junction of the projectile tail and the cylindrical part is more serious. In a certain range, the larger the bending angle, the greater the velocity difference before and after the expansion wave, the greater the velocity, the lower the pressure, the larger the tail cone angle, and the smaller the pressure coefficient of

the projectile tail, that is, the absolute value of the pressure coefficient. bigger. At the same time, it can be seen that after the expansion wave of the projectile tail, the pressure coefficient of the projectile tail is negative as a whole, which means that the larger the tail cone angle is, the greater the drag coefficient of the projectile tail is. Moreover, as the Ma number increases, the absolute value of the pressure coefficient of the projectile tail will further increase, that is, the tail resistance will also gradually increase.

4.3 Variation of Projectile Drag Coefficient

According to the above analysis, the drag coefficient of the projectile tail is divided into two parts: bottom resistance C_b and tail resistance C_w. The bottom resistance C_b decreases with the increase of the tail cone angle, and the tail resistance C_w increases with the increase of the tail cone angle. It is conceivable that there must be an intersection point between the bottom resistance C_b curve and the tail resistance C_w curve, so that the resistance coefficient of the projectile tail is the smallest, that is, when the projectile head and the cylindrical part are constant, the projectile resistance coefficient Cd is the smallest.

Fig. 11 shows the variation curve of correlation coefficient with tail cone angle. It can be seen that under different Ma numbers, the tail cone angle that minimizes the drag coefficient C_d of the projectile is different, which is called the optimal tail cone angle, which is constructed according to the simulation results. The relationship between optimal tail cone angle and Ma number shown in Fig. 12.

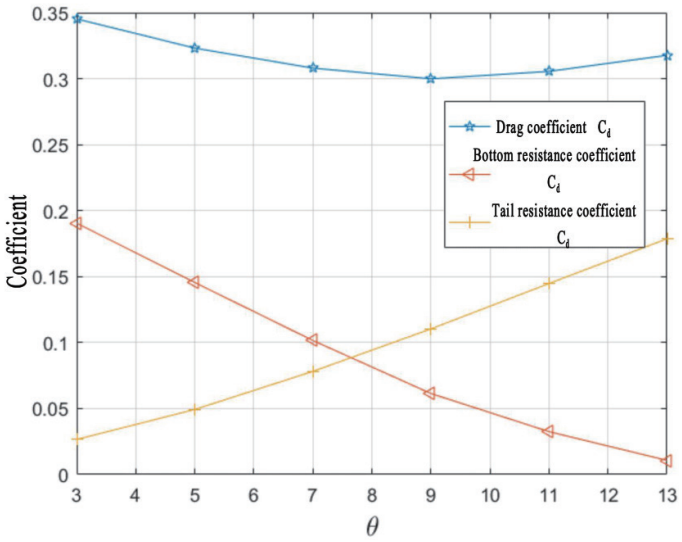

(a) Ma=1.5

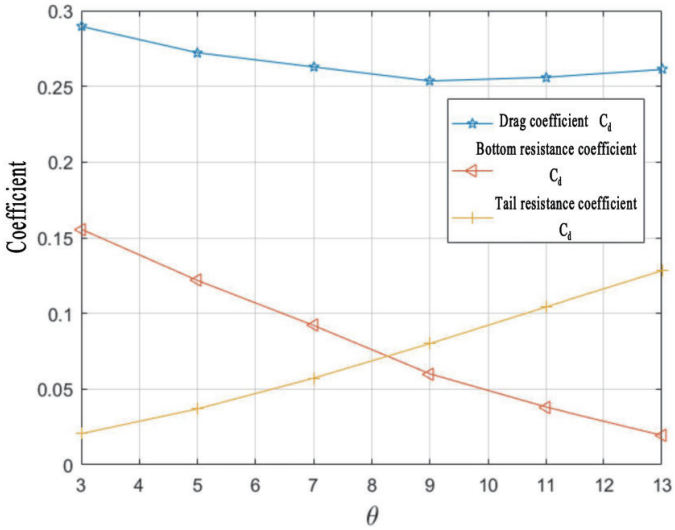

(b) Ma=2

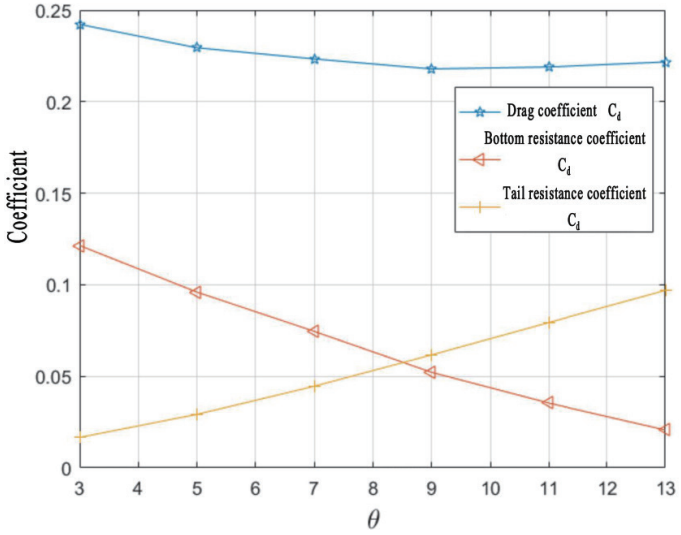

(c) Ma=2.5

Fig. 11. Correlation coefficient versus tail cone angle θ

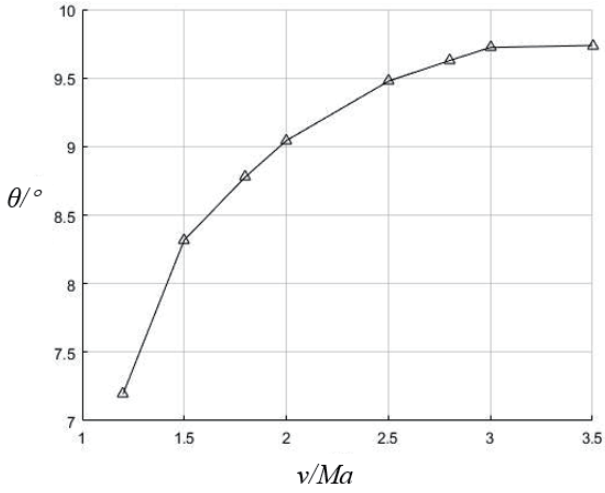

Fig. 12. Relationship between optimal tail cone angle and Ma number

It can be observed from Fig. 12 that the optimal tail cone angle increases with the increase of Ma number, but its increasing speed gradually decreases with the increase of Ma number. When Ma number is greater than 3, the optimal tail cone angle changes. It is extremely small, and the overall approach is 9.8°, that is, as the Ma number increases, the variation of the optimal tail cone angle with the Ma number decreases. When the Ma number is greater than 3, it can be considered that the optimal tail cone angle is a fixed value, for the SOCBT projectile, the optimal tail cone angle greater than 3Ma is about 9.8°.

5 Conclusion

The drag coefficient of the stern-shaped projectile tail is affected by the shape of the stern. The increase of the tail cone angle increases the pressure coefficient of the tail and the tail resistance. With the increase of the tail cone angle, the action area of the bottom pressure decreases, and the absolute value of the bottom pressure coefficient also decreases. The combined effect of the two causes the bottom resistance coefficient to decrease with the increase of the tail cone angle. The tail cone angle also affects the airflow velocity at the end of the projectile and the separation angle of the boundary layer, affects the airflow at the bottom of the projectile, changes the pressure coefficient at the bottom of the projectile, and affects the bottom resistance coefficient of the projectile.

When the tail length is constant, the tail resistance increases with the increase of the tail cone angle, and the

bottom resistance decreases with the increase of the tail cone angle. The combined effect of the two makes the overall drag coefficient have a minimum value, and the corresponding tail cone angle is 7°~10°, and the flight speed of the projectile increases, the effect of the flight speed is smaller, that is, with the increase of Mach number, the size of the optimal tail cone angle of the stern shape of the projectile tends to be stable. When the flight speed is greater than 3Ma, the optimal tail angle The size of the cone angle does not change. Finally, finite element analysis and numerical research on the aerodynamic shape of the ship-shaped tail projectile with other special shape parameters or other structural forms would be carried out.

References

[1] H.-B. Lu, S.-Z. Zhuansun, F.-W. Su, Y.-W. Li, Research on Influence of Base Cavity with Different Shape on Aerodynamic Drag of Projectile, Journal of Projectiles, Rockets, Missiles and Guidance 36(5)(2016)112-114+141.
[2] H.-B. Xuan, W.-J. Zhang, Y. Yu, J. Hu, Numerical Study on Drag Reduction of Projectile in Subsonic and Transonic Speed, Chinese Journal of Ordnance Equipment Engineering 38(11)(2017)1-8.
[3] M.-J. Molezzi, J.-C. Dutton, Study of subsonic base cavity flowfield structure using particle image velocimetry, AIAA Journal 33(2)(1995) 201-209.
[4] H. Xiong, Aerodynamic Characteristics Calculation and External Ballistic Simulation of Bullet, [dissertation] Taiyuan: North University of China, 2019.
[5] W. Jiajan, R.S.M. Chue, T. Nguyen, S.C.M. Yu, Boattail juncture shaping for spin-stabilized rounds in supersonic flight, Shock Waves 25(2)(2015) 189-204.
[6] H.-B. Lu, J. Gao, Research on Shrinkage Shape of Base Cavity Upon Aerodynamic Drag of Projectile, Journal of Ordnance Equipment Engineering 40(6)(2019) 5-9.
[7] J.-G. Shi, L.-P. Xie, Numerical simulation and analysis of 3D flow field for high spinning base bleed projectile, Journal of Ordnance Engineering 38(6)(2017) 1090-1096.
[8] D. Regodic, A. Jevremovic, D. Jerkovic, The prediction of axial aerodynamic coefficient reduction using base bleed, Aerospace Science and Technology 31(1)(2013) 24-29.
[9] C.-Y. Wang, Z.-H. Wang, X.-H. Yang, Computational fluid dynamics and its parallel algorithms, Changsha, National University of Defense Technology Press, 2000 (ISBN: 7810246127).
[10]Y.-X. Ren, H.-X. Chen, Fundamentals of Computational Fluid Dynamics, Beijing: Tsinghua University Press, 2006 (7-11, ISBN: 7302130043).
[11]B.-B. Chen, Z.-H. Luo, Z.-H. Yuan, X.-L. Jiang, B. Chen, Numerical Investigation on Magnus Effect of a Spinning Projectile, Advances in Aeronautical Science and Engineering 9(2)(2018) 184-190.
[12]W.B. Sturek, H.A. Dwywr, L.D. Kayser, C.J. Neitubicz, R.P. Reklis, K.O. Opalka, Computations of magnus effects for a yawed, spinning body of revolution, AIAA Journal 16(7)(1978) 687-692.
[13]M.-C. Miller, Surface pressure measurements on a transonic spinning projectile, Journal of Spacecraft and Rockets 22(2) (1985) 112-118.
[14]W.-C. Chen, Calculation and Optimization of Aerodynamic and Exterior Ballistics Characteristics of Spinning Projectile, [dissertation] Nanjing: Nanjing University of Science and Technology, 2012.
[15]D.R. Chapma, An analysis of base pressure at supersonic velocities and comparison with experiment, NACA TR 1051, 1951.
[16]X.-J. Shi, A Study of Aerodynamic Character of Projectile under the Different Base Bleed Parameters, [dissertation] Nanjing: Nanjing University of Science and Technology, 2007.
[17]J.-T. Wang, A Model for Base Pressure Analysis of Base Bleed Projectile/Missile and Simulated Calculation, [dissertation] Nanjing: Nanjing University of Science and Technology, 2015.